Co-precipitation synthesis control for sodium ion adsorption capacity and cycle life of copper hexacyanoferrate electrodes in battery electrode deionization

Le Shi [a], Xiangyu Bi [a], Evan Newcomer [a], Derek M. Hall [b], Christopher A. Gorski [a], Ahmed Galal [c], Bruce E. Logan [a],[*]

[a] *Department of Civil and Environmental Engineering, The Pennsylvania State University, University Park, PA 16802, USA*
[b] *Department of Energy and Mineral Engineering, The Pennsylvania State University, University Park, PA 16802, USA*
[c] *Chemistry Department, Faculty of Science, Cairo University, 12613 Giza, Egypt*

ABSTRACT

Prussian blue analogues are being explored as electrode materials for electrochemical desalination of saline water in battery-type electrode deionization systems and hybrid capacitive deionization systems due to their open framework crystal structure that provides selective adsorption of multiple cations, high theoretical sodium adsorption capacities, and low costs. However, poor electronic conductivity and instability (dissolution) prevents the use of these materials for long-term desalination applications. To understand how synthesis conditions might improve the properties of copper hexacyanoferrate (CuHCF) powders relative to sodium ion adsorption capacity and cycle life, the co-precipitation process was investigated using multiple common synthesis strategies that included addition of chelators and sodium salts as well as different concentrations and oxidation states of precursors. Smaller crystallite sizes (<35 nm) and lower structural water contents increased the initial sodium removal capacity to 53.2 mAh/g from 40.4 mAh/g (control), but also reduced cycling stability in long-term operation (20–55% retention over 100 cycles). The trade-off in stability is thought to be a consequence of structural water facilitating ion diffusion within the material. Adding chelators as precursors led to a highly reversible Cu^{II}/Cu^{I} redox couple that increased the stability of the Fe^{III}/Fe^{II} redox couple in BDI cycling performance (79.4% retention over 100 cycles).

1. Introduction

Electrochemical deionization technologies, such as capacitive deionization (CDI), have been rapidly developed by using similar electrodes designed for supercapacitors to achieve selective removal of specific ions.[1–5] Cell architectures being examined to improve CDI performance include flow-by or flow-through electrodes,[6] symmetric or asymmetric electrodes,[7] single or multiple channels,[8,9] and fixed or flowing electrodes.[10] Another approach to improve performance is using active materials with higher sodium ion adsorption capacities and longer cycling lifetimes than purely capacitive materials.[2] Battery electrode deionization (BDI) was recently focused to improve the CDI process for brackish water desalination by utilizing battery-type materials (intercalation material) to replace capacitive-based electrodes, which substantially improved sodium adsorption capacity and

thermodynamic energy efficiencies compared to pure carbon-based materials.[2,11,12]

Battery electrode materials such as Prussian blue analogues (PBAs) have an open framework crystal structure that can store sodium ions within their crystal lattice.[13] PBAs can be prepared from abundant and non-toxic precursors of a metal salt and a hexacyanoferrate complex, by an easy, low-cost and scalable co-precipitation process. Metal sulfates, nitrates, or chlorides are used for the metal salt precursor and $A_3Fe^{III}(CN)_6$ or $A_4Fe^{II}(CN)_6$ are used for the hexacyanoferrate precursor, where A is usually potassium or sodium. Although co-precipitation methods have been widely adopted for PBAs material preparation, there is a general lack of fundamental understanding of the nucleation and growth mechanism of PBAs during this co-precipitation process. [14]

A range of commonly used conditions used to synthesize PBAs for

---

producing aqueous sodium ion batteries include varying precursor concentrations[15] and flowrates,[16] atmospheric conditions during co-precipitation,[17] aging time after the precipitation process,[18] and the inclusion of additives, such as sodium pyrophosphate and sodium citrate.[18,19] Slight differences in these synthesis conditions can substantially impact the properties of the precipitation products, such as particle sizes and shapes, ion composition, and water content, which can impact electrochemical performance when these materials are used as electrodes in energy storage systems.[20] Therefore, a better understanding of the impact of these different synthesis conditions on the sodium ion adsorption capacity and cycle life of the PBAs is needed to optimize the electrode materials for BDI applications that use much lower concentrations of salts in feed solutions than those in energy storage systems.

Copper hexacyanoferrate (CuHCF) was investigated here as a model PBA because it has shown promising performance in brackish water and wastewater deionization applications but poor stability.[11,21–23] A systematic study of the effects of synthesis conditions on materials properties and their electrochemical deionization performance was investigated by varying the reagent concentration, metal oxidation state, atmospheric conditions, aging time, and the inclusion of chelator or sodium salts additives. These different synthesis parameters were varied to determine their impacts on BDI performance in terms of sodium ion adsorption capacity and cycling stability over time. To understand differences in stability and performance we examined the properties of pristine powders in terms of their crystallinity and elemental composition using powder X-ray diffraction (XRD), inductively coupled plasma atomic emission spectrometry (ICP-AES), morphology and particle size using scanning electron microscopy (SEM), and water content using thermogravimetric analyses (TGA). The electrochemical characterization of each sample with cyclic voltammetry (CV) and electrochemical impedance spectroscopy (EIS) was used to analyze the sodium adsorption behavior.

2. Experimental section

2.1. Materials synthesis

Copper hexacyanoferrate powders (CuHCF) were produced using a co-precipitation method under several different conditions using: $Cu(NO_3)_2 \cdot 2.5H_2O$ (Sigma-Aldrich) with or without the chelator (Solution A), and $K_3Fe(CN)_6$ (EMD Chemicals) or $K_4Fe(CN)_6$ (Sigma-Aldrich) with or without the chelator and NaCl (Sigma-Aldrich) (Solution B). Different synthesis conditions included precursor concentrations, precursor oxidation states, chelator types and concentrations, the use of air or nitrogen atmosphere, and additional sodium salt as summarized in Table 1. The Group 1 sample was control without any additives in precursors. Samples in Groups 1 and 2 used a solution B of $K_3[Fe(CN)_6]$ and an air atmosphere. Samples in Group 2 used $Na_4P_2O_7$ (Sigma-Aldrich) in solution A (Cu + SP) and PVP-10 (polyvinypyrrolidone, average mol wt 10,000, Sigma-Aldrich) and NaCl in solution B (Fe^{3+}+Na). Samples in Group 3 and Group 4 used $K_4[Fe(CN)_6]$ in solution B and a nitrogen atmosphere. Samples in Group 3 had contained $Na_4P_2O_7$ in solution B (Fe^{2+}+SP) or in both A (Cu + SP) and B solutions (Fe^{2+}+SP). Samples in Group 4 had additives of $Na_3C_6H_5O_7$ (Fisher Scientific) in solution B (Fe^{2+}+SC) or in both solutions A (Cu + SC) and B (Fe^{2+}+SC). Solutions of A or B were added dropwise into deionized (DI) water using a peristaltic pump (0.5 mL/min) at room temperature. Bottles were wrapped with aluminum foil to prevent light exposure. Solutions A and B in sample 3 and 4 were bubbled with N_2 to protect Fe^{2+} from oxidation. Precipitates collected after 1 or 5 days were washed several times with ethanol and DI water by centrifugation. The products were collected and dried in a vacuum oven (70 °C) for 12 h. The dry powders were ground carefully using a mortar and pestle.

2.2. Material characterizations

To quantify the elemental composition of the samples, the prepared

Table 1
Different synthesis conditions for CuHCF samples separated into 4 main groups by number, with additional subgroupings indicated by a lower case letter. The subscripts H, M and L indicate high, medium and low concentrations of the indicated reagents.

Samples by Group	Solution	Reagents	Concentration (M)	Atmosphere	Aging time (d)
1: $(Cu_H)[A]+(Fe_M{}^{3+})[B]$	A	$Cu(NO_3)_2$	0.1	Air	1
	B	$K_3[Fe(CN)_6]$	0.05		
2a: $(Cu_L + SP)[A]+(Fe_L{}^{3+}+Na_H)[B]$	A	$Cu(NO_3)_2$	0.008	Air	5
		$Na_4P_2O_7$	0.008		
	B	$K_3[Fe(CN)_6]$	0.003		
		PVP-10	0.06 g/L		
		NaCl	0.8		
2b: $(Cu_M + SP)[A]+(Fe_M{}^{3+}+Na_H)[B]$	A	$Cu(NO_3)_2$	0.05	Air	5
		$Na_4P_2O_7$	0.05		
	B	$K_3[Fe(CN)_6]$	0.02		
		PVP-10	0.06 g/L		
		NaCl	0.8		
2c: $(Cu_M + SP)[A]+(Fe_M{}^{3+}+Na_L)[B]$	A	$Cu(NO_3)_2$	0.05	Air	5
		$Na_4P_2O_7$	0.05		
	B	$K_3[Fe(CN)_6]$	0.02		
		PVP-10	0.06 g/L		
		NaCl	0.2		
3a: $(Cu_M + SP)[A]+(Fe_M{}^{2+}+SP)[B]$	A	$Cu(NO_3)_2$	0.05	N_2	1
		$Na_4P_2O_7$	0.05		
	B	$K_4[Fe(CN)_6]$	0.05		
		$Na_4P_2O_7$	0.05		
3b: $(Cu_M)[A]+(Fe_M{}^{2+}+SP)[B]$	A	$Cu(NO_3)_2$	0.05	N_2	1
	B	$K_4[Fe(CN)_6]$	0.05		
		$Na_4P_2O_7$	0.05		
4a: $(Cu_M + SC)[A]+(Fe_M{}^{2+}+SC)[B]$	A	$Cu(NO_3)_2$	0.05	N_2	1
		$Na_3C_6H_5O_7$	0.05		
	B	$K_4[Fe(CN)_6]$	0.05		
		$Na_3C_6H_5O_7$	0.05		
4b: $(Cu_M)[A]+(Fe_M{}^{2+}+SC)[B]$	A	$Cu(NO_3)_2$	0.05	N_2	1
	B	$K_4[Fe(CN)_6]$	0.05		
		$Na_3C_6H_5O_7$	0.05		

powders were decomposed in aqua regia by microwave digestion. Powder (0.05 g) was placed in Teflon-lined vessels and hydrochloric acid (9 mL HCl, trace metal grade, 35–38% Fisher Scientific) and nitric acid (3 mL HNO_3, trace metal grade, VWR, 67–70%) were added into each vessel and reacted for 30 min at room temperature. Vessels were then heated in a microwave oven (MARS 6, CEM) at 220 °C for 30 min. The mixtures were dried and diluted with 2% HNO_3 solution to reach an appropriate concentration range for subsequent analysis using inductively coupled plasma atomic emission spectrometry (ICP-AES, iCAP 7400, Thermo Fisher Scientific). High purity standards were used to calibrate the results. All tests were conducted in duplicate.

Powder X-ray diffraction patterns were recorded using a powder diffractometer (Malvern Panalytical Empyrean) with a Cu Kα ($\lambda_1 = 1.5406$ Å, $\lambda_2 = 1.5444$ Å) radiation source, at an accelerating voltage of 45 kB and current of 40 mA. Scans were operated between 10 and 60° (2θ) with a nominal step size of 0.026°/s. Phase ID was carried out using Jade software from Materials Data Inc (MDI). The morphology of particles in samples was analyzed using scanning electron microscopy (SEM, Verios G4, Thermo Fisher Scientific). Due to the insufficient electronic conductivity of the synthesized particles, Iridium (5 nm) was coated on the samples before scanning and the backscattered electron mode was employed using an acceleration voltage of 5 kV and a beam current of 0.2nA. The thermal stability, dehydration temperature and water content of each sample were analyzed with a thermogravimetric analyzer (TGA, NETZSCH STA 449F3, Selb) under a flowing N_2 gas atmosphere at 25 to 600 °C (10 °C/min) with the sample placed in crucible (Al_2O_3 85 μl).

2.3. Electrode fabrication

Electrodes were prepared by painting the CuHCF slurries onto carbon cloth (7 cm^2 of catalyst area of 11 cm^2 total cloth area, cloth thickness of 0.356 mm and density of 1.5 g/cm^3, AvCarb 1071 HCB, AvCarb Material Solutions). The carbon cloth was cleaned before use by soaking in HNO_3 (1 M), DI water, and then ethanol (70%) with sonication (20 min each solution) and heated at 450 °C in an oven overnight. The CuHCF slurry consisted of synthesized active material (CuHCF), carbon black (Vulcan XC72R, Cabot, average particle size = 50 nm), and polyvinylidene fluoride (PVDF, Kynar HSV 900, Arkema Inc.) in a mass ratio of 8:1:1 in 1-methyl-2-pyrrolidinone (NMP, Sigma-Aldrich, 0.5 mL for each). The active material and carbon black were mixed and ground with a mortar and pestle and then NMP containing dissolved PVDF was added into the mixture with continuous grinding. The total mass loading of the resulting CuHCF electrodes was ~ 6 mg/cm^2. The counter electrodes for the pre-conditioning, CV and EIS tests were prepared by the same method except activated carbon (AC, YP-50F, Kuraray Chemical) used in place of CuHCF powders. The coated electrodes were dried on a hotplate at 70 °C for 30 min and then in a vacuum oven at 70 °C for 12 h.

2.4. Battery deionization performance

A pair of electrodes containing identical CuHCF materials were used for deionization tests with a lab-made flow cell system constructed as previously reported.[21] Before deionization performance tests, the potentials of the two CuHCF electrodes were adjusted to different states of charge to optimize their performance for Na^+ ion uptake. The two CuHCF electrodes were set to 0.4 V or 1.0 V (vs Ag/AgCl in 3 M NaCl) as a working electrode in a three-electrode system, with AC coated carbon cloth as a counter electrode and a reference electrode (Ag/AgCl, 3 M NaCl) in a 1 M NaCl electrolyte. A constant current of ± 7 mA/30 mg (normalized by the mass of active material) was applied until the predetermined cut-off potential (0.4 and 1.0 V) was reached and then followed by the charging with constant potential of 0.4 or 1.0 V for 20 min. The sodium-enriched electrode was placed as the anode and the sodium-depleted electrode was placed as the cathode in the BDI flow cell system, with the two chambers separated by an anion exchange

membrane (AEM, 106 ± 1 μm thick with an ion exchange capacity of 1.85 mmol/g, Selemion AMV, Asahi Glass). A fabric spacer (0.28 mm thick and 33% porosity; Sefar Nitex, 06–210/33) was placed between the electrode and AEM. A constant current of 7 mA/30 mg (normalized by the mass of active material) was applied in the voltage window of ± 0.6 V. Feed solution was 50 mM NaCl as synthetic brackish water with a flow rate of 0.5 mL/min by a peristaltic pump at room temperature.

2.5. Electrochemical characterization

All electrochemical measurements were carried out with a Bio-logic VMP3 potentiostat, in three-electrode cells consisting of a CuHCF electrode as the working electrode, AC as the counter electrode, and a Ag/AgCl reference electrode (3 M NaCl, +0.209 V with respect to SHE). Before each electrochemical test, the prepared electrodes were immersed in 1 M NaCl solution in a vacuum desiccator for 20 min to remove gas bubbles attached on the surface of electrode. Cyclic voltammetry (CV) scans were obtained from –0.3 to 1.0 V, and galvanostatic charge and discharge tests were conducted over a range of 0 to 1 V in 1 M NaCl without IR correction. Electrochemical impedance spectroscopy (EIS) was carried with the frequency range from 2 mHz to 500 kHz with amplitude of 5 mV at open circuit potential (OCP). All EIS measurements were performed allowing the electrodes to rest at their open circuit potential (OCP) values for 10 min.

3. Results and discussion

3.1. Impact of preparation methods on stability and performance

To investigate the cycling performance in a BDI flow cell system of each CuHCF sample, a potential window of ± 0.6 V was used to focus on the Fe^{III}/Fe^{II} redox couple reaction (Fig. 1). The highest capacity retention was 79.4 % after 100 cycles for sample 2a. The capacity retention, normalized to the initial capacity for each sample, was decreased to 55.5% (sample 4b), 45.6% (sample 4a), 39.6% (sample 3b), and 20.7% (sample 3a), after 100 cycles (Fig. 1). The capacity retention without normalization are in the SI for a subset of samples (Figure S1). Charge-discharge efficiency was also impacted with a higher efficiency observed for sample 2a and 2b compared to other samples likely due to the enhanced reversible Fe^{III}/Fe^{II} redox reaction than others. These results showed that the combination of materials and fabrication methods used for sample 2a produced the most stable electrodes. The reasons for this improved performance were examined through an analysis of the materials in terms of surface and morphological properties such as particle size, types of water content, and electrochemical characteristics of the electrodes.

3.2. Morphological and structural properties

Powder X-ray diffraction (XRD) patterns obtained for the different CuHCF pristine powders (Fig. 2) indicated the presence of similar and highly crystalline materials. The main peaks in the spectra corresponded to those reported for $A_{2-x}M[Fe(CN)_6]_{1-y}\cdot\square_y\cdot zH_2O$ (A is an insertion ion, M is the transition metal and a blank box is a vacancy), indicating the cubic framework with Fe^{III} was octahedrally linked with CN^- groups that produced the open framework structure needed for large channels to accommodate cation intercalation.[24] A change in the peak intensity ratio of I_{220}/I_{200} was observed among the samples. An increase in the I_{220}/I_{200} peak ratio indicates a larger concentration of alkaline ions within the CuHCF crystal structure. Additional alkaline ions reduce Cu–N bond distance and affect the electronic structure of the Fe in the crystal.[15,24,25] The change in the I_{220}/I_{200} peak ratio was consistent with the stoichiometry composition of each sample determined by ICP-OES (Table S1). A higher concentration of alkaline ions were found when chelators or NaCl were present in the precursors of samples 2–4, while the smallest I_{220}/I_{200} intensity of sample 1 was a result of no extra
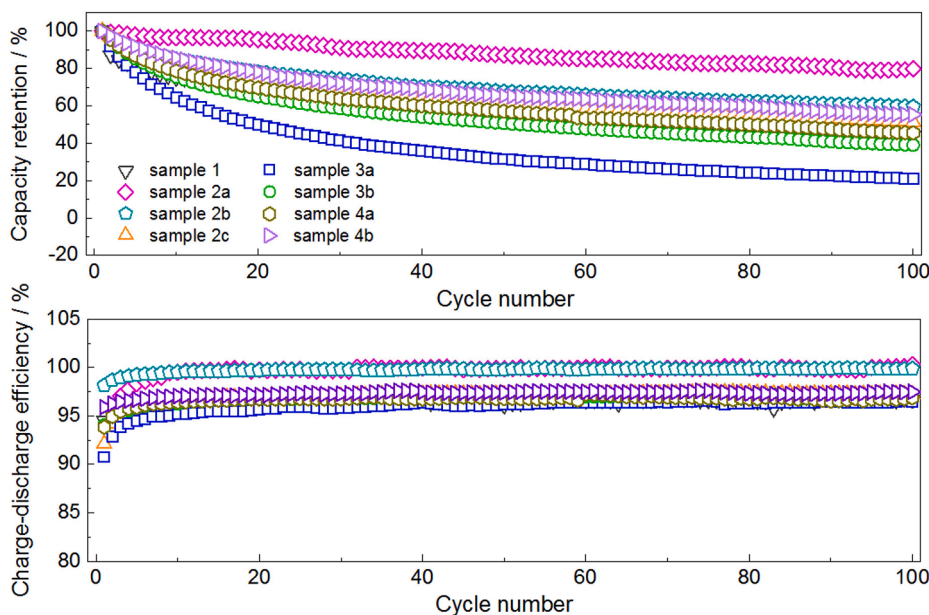
Fig. 1. Cycling performance of CuHCF-based electrodes with powder sample 1–4 over 100 cycles in the BDI flow cell with 50 mM NaCl feed solution. A constant current of 7 mA/30 mg was applied in the voltage window of ± 0.6 V with a flow rate of 0.5 mL/min.
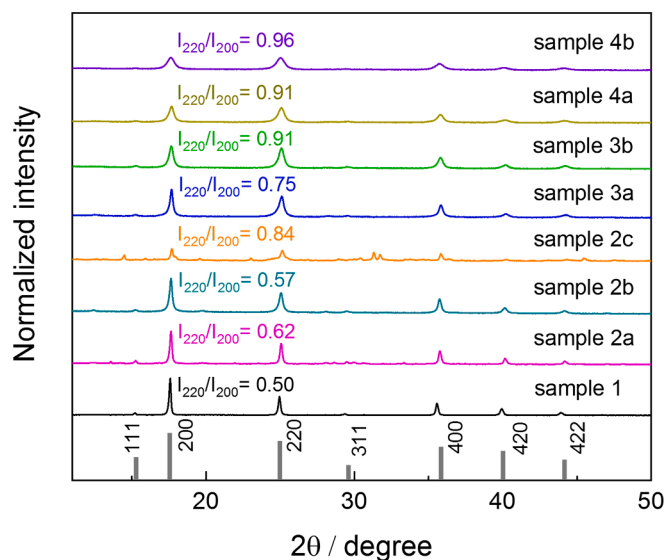

Fig. 2. Powder X-ray diffraction (XRD) spectra of CuHCF pristine powders prepared under different conditions (sample 1–4).

alkaline ions addition in the precursors. CuHCF powders synthesized with metal salts in different oxidation states produced differently shaped peaks. Sharper peaks were observed (Fig. 2) for the CuHCF samples prepared with the oxidized form $[Fe(CN)_6]^{3-}$ (samples 1 and 2) compared to CuHCF samples prepared with the reduced form $[Fe(CN)_6]^{4-}$ (samples 3 and 4). The broader peaks of the reduced form (samples 3 and 4) compared to the oxidized form (samples 1 and 2) suggested that the reduced samples had smaller crystallite sizes,[16,24] which was confirmed based on the decreased calculated crystallite size using peak width at the half-maximum intensity of peaks (2 0 0) in the Scherrer formula (Table S2). The smaller crystallite sizes of samples 3 and 4 could also be due to the shorter aging time than samples 2. As observed in the SEM images, samples with smaller crystallite sizes such as 4a (21.1 nm) and 4b (14.8 nm) tended to show aggregation into larger particles (Figure S2).

Water contents of the CuHCF pristine powders were measured using

TGA (Fig. 3). Based on the rate of weight loss, water content was classified into three types of water content in the PBA framework: surface adsorbed, zeolitic, and coordinated. The adsorbed water on the particle surface was removed first followed by zeolitic or interstitial water located in the interstitial sites of the crystal framework, and lastly the water chemically coordinated with the transition metal ions. These different types of water content are indicated by different colors in Fig. 3, with results summarized in Table S3. Generally, the weight loss due to surface water occurred below 200 °C, zeolitic water followed by coordinated water loss occurred at temperatures of 200 to 400 °C, and the weight loss by thermal decomposition at higher temperatures. [20,26] The coordinated water bonds with Fe ions in PBA framework required higher temperature to volatilize, which might affect the surrounding electronic states of the Fe ions or the $Fe(CN)_6$ groups. [20,27,28] It was found that the amount of zeolitic water decreased significantly from 12.3% (sample 1, Fig. 3a) to 6.2% − 8.2% (among sample 2–4, Fig. 3b-h) due to additional chelators or sodium added into the precursor solutions. This result showing a higher water content of alkaline-free than alkali-rich Prussian blue is consistent with the previous reports.[29] The amount of coordinated water increased from 3.9% in Sample 1 to higher values in sample 2 of 6.1% (2c) 13.6% (2a), and 13.8% (2b), with no substantial weight loss observed from coordinated water for samples 3 and 4 containing reduced oxidation state of iron ($[Fe(CN)_6]^{4-}$). The reasons for the increased amount of coordinated water in these samples were not clear but further investigation could lend additional insight into improving the performance of these materials.

3.3. Electrochemical properties

CV curves were obtained for CuHCF-based electrodes with each powder sample, revealing different redox couples and level of activities in each sample (Fig. 4). The peaks of O1/R1 pair at higher potentials (0.5–0.8 V) corresponded to the oxidation/reduction of Fe^{III}/Fe^{II}, and the O2/R2 pair at lower potential (~0.2 V) was attributed to Cu^{II}/Cu^{I}. [30,31] The pair of Cu^{II}/Cu^{I} redox peaks became more pronounced in samples with the addition of chelators and sodium (Fig. 4b-h) compared to the sample without any additives (Fig. 4a). The activation of Cu^{II}/Cu^{I} redox reaction in CuHCF could be affected by multiple factors, such as chelators in precursors,[19] and presence of the abundant lattice water in the framework.[31] The activation of Cu^{II}/Cu^{I} redox reaction in
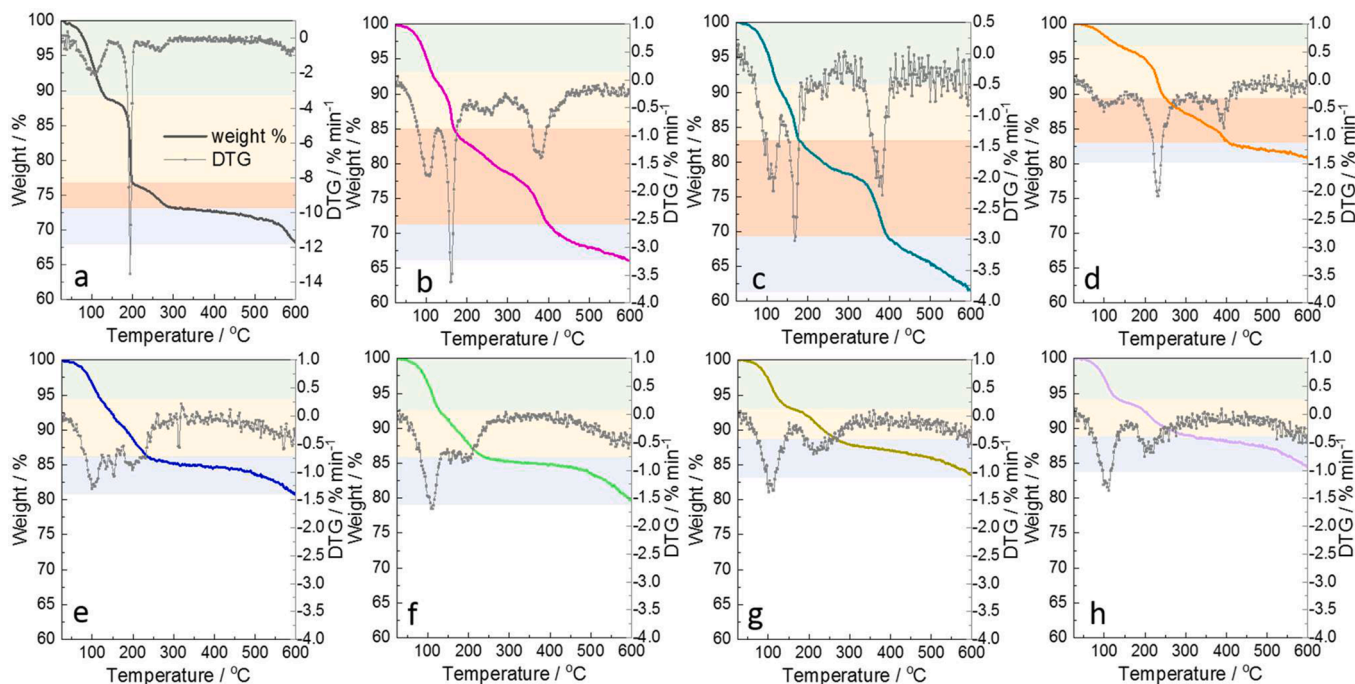
Fig. 3. Thermogravimetric analyses (TGA) of CuHCF pristine powders (a-sample 1, b-sample 2a, c-sample 2b, d-sample 2c, e-sample 3a, f-sample 3b, g-sample 4a and h-sample 4b). Different background colors indicated for different forms weight loss (green-surface adsorbed water, yellow-zeolitic water, orange-coordinated water and blue-thermal decomposition).
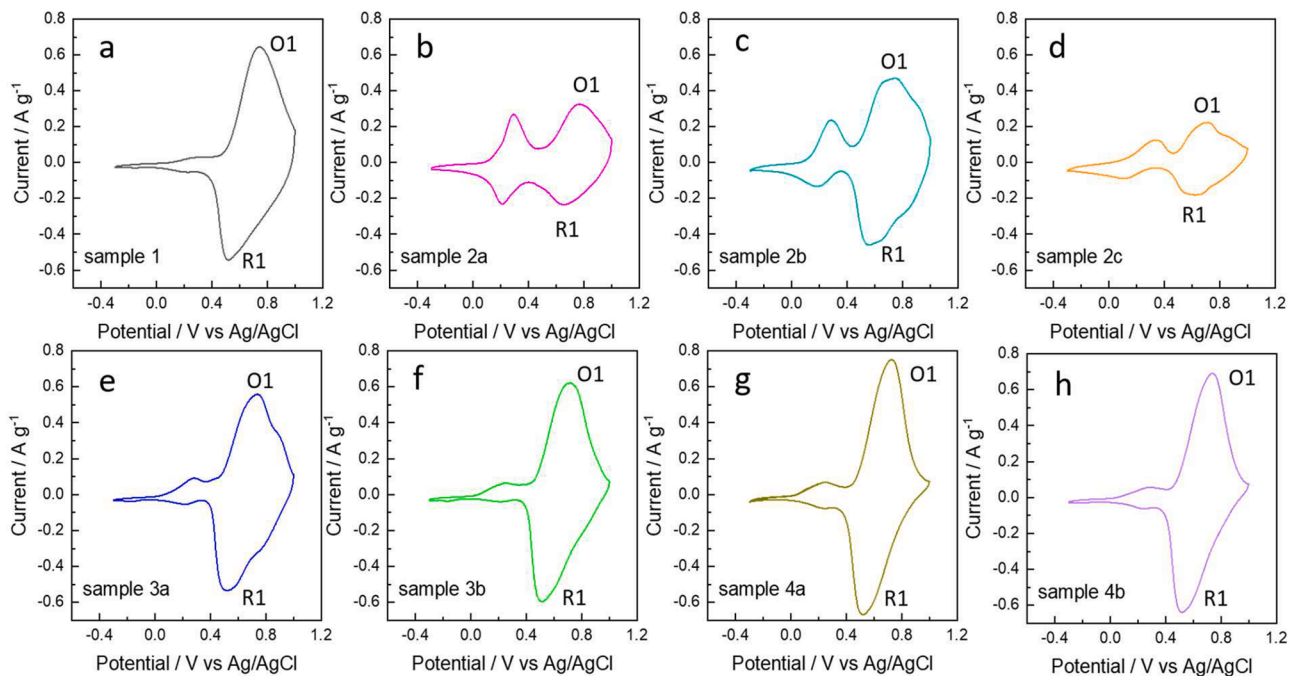
Fig. 4. Cyclic voltammetry (CV) of CuHCF-based electrodes with each powder sample with scan rate of 1 mV/s in the potential window of −0.3 to 1.0 V in 1 M NaCl solution (a-sample 1, b-sample 2a, c-sample 2b, d-sample 2c, e-sample 3a, f-sample 3b, g-sample 4a and h-sample 4b).

sample groups 2–4 was likely due to the surface adsorbed chelates ions from the precursor solution.[19] During the crystallization process, the chelator ions can be adsorbed onto the metal cation surfaces because the pyrophosphate ions ($P_2O_7^{4-}$) in sodium pyrophosphate or carboxylate groups (–COOH) in sodium citrate could form strong covalent interaction with Cu cations.[18,19] The most active Cu^{II}/Cu^{I} redox reaction was found for sample 2a, which might due to the lowest concentration of

metal salt ions in the precursor, providing a better contact between chelators and Cu ions. The peak-to-peak separation between the Fe^{III}/Fe^{II} (O1 and R1) peaks (Table S4) was smaller for samples 2a (0.114 V), 2b (0.171) and 2c (0.093 V) compared to sample 1 (0.221 V). The smaller separation between the peaks could indicate either a faster and more reversible electron transfer processes or faster diffusion rates. The CV curves for samples 1 and 2a were obtained at various scan rates (0.05

– 1 mV/s in 1 M NaCl) (Figure S3), with the peak current of each redox reaction used to calculate exponent b in the equation $i = av^b$ (SI). The b value of 0.5 indicates a typical intercalation process limited by a semi-infinite linear diffusion process, while a b value of 1 indicates a surface-controled process. The b values for R1 and R2 peaks for both samples were close to 1, indicating either surface-controlled process contributed to Na$^+$ removal or a fast faradaic process with minimal diffusion limitations occurred due to the small particle size of the active material.[32,33] The CV scans at faster rates (1 – 20 mV/s in 1 M NaCl) were also obtained for sample 2a (Figure S3) to confirm the reversibility of the second redox reaction from Cu^{II}/Cu^I. The peaks for Cu^{II}/Cu^I were also clearly observed as scan rates increased to 20 mV/s. However, the peaks positions shifted as scan rates increased likely due to irreversible ohmic polarization effects.[34,35] The CV curves after BDI cycling were also obtained for a subset of samples (Figure S4). The sample with higher cycling stability showed fewer changes on peaks of Fe^{III}/Fe^{II} and the samples with lower cycling stability showed bigger changes on peaks of Fe^{III}/Fe^{II} (Figure S4).

Solid-state ion diffusion (within the electrode material) in each sample can be characterized by the ion diffusion coefficient (D) calculated from EIS data (Fig. 5). For typical intercalation materials the Nyquist plot contains a depressed semi-circle with an inclined straight line.[36] The Warburg impedance, Z_W, is calculated from the straight line in the low-frequency region of a Nyquist plot. The Warburg coefficient (σ) for each sample was therefore obtained from the slope of a plot of Re(Z) versus $\omega^{-1/2}$ in the same region as the Warburg impedance (Figure S5), and the ion diffusion coefficient (D) was calculated from σ and other constants as described in the supporting information.[37] The diffusion coefficients for samples 1 (1.45×10^{-8} cm^{2}s^{-1}), 2a (4.78×10^{-8} cm^{2}s^{-1}) and 2b (6.56×10^{-10} cm^{2}s^{-1}) were 10–1000 times larger than the other samples (range of 1.08×10^{-11} to 8.49×10^{-11} cm^{2}s^{-1}) (Table S5). A larger diffusion coefficient for the 1, 2a and 2b samples suggests high coordinated water content in the CuHCF framework could promote ion diffusion within the materials, but the impact of coordinated water on ion diffusion is not clear (Fig. 3). A previous study suggested that ion diffusion in the PBA solid material was assisted by coordinated water via a paddlewheel mechanism, in which the guest ions moved through channels and vacancies.[38] However, another

reached the opposite conclusion due to results that PBAs without coordinated water in the framework showed excellent cycling stability in a sodium-ion battery.[28] The role of water content in PBA framework for ionic conduction therefore is poorly understood, making it difficult to use water content as a design parameter in production of PBA materials for different applications.[14]

3.4. Battery deionization performance

Galvanostatic charge and discharge profiles of the different CuHCF-based electrodes were used to assess their sodium removal (charge storage) capacities (Fig. 6). During the discharge step, there was a first recognizable plateau (1.0 – 0.5 V vs Ag/AgCl) corresponded to the Fe^{III}/Fe^{II} cathodic peak for all samples. A second plateau (0.4 – 0.0 V vs Ag/AgCl) was more visible and pronounced for sample 2, that likely were due to the Cu^{II}/Cu^I cathodic peaks identified in CVs in Fig. 4. Further support for the presence of these two peaks was shown by the plot of differential capacitive curve (dQ/dV versus V, Figure S6). Sample 2 showed higher activity of Cu^{II}/Cu^I redox reaction as shown with higher peak of differential capacity (Figure S6) consistent with the CV results (Fig. 4).

Sample 2a had an increased sodium adsorption capacity by 49% (60.2 mAh/g) compared to sample 1 (40.4 mAh/g) during the discharge step in the potential window of 1 – 0 V (vs Ag/AgCl) (Fig. 6). The increase of capacity suggested that chelators enabled CuHCF to have both Cu and Fe redox-active centers for sodium intercalation.[18] Despite an activated Cu redox site in sample 2c, the ion capacity (25.5 mAh/g) was not increased compared to sample 1, which could be attributed to its large crystal and particle size (Figure S2 and Table S3) for sample 2C, leading to longer diffusion paths or a kinetic barrier for diffusion. [39,40] The bigger sodium adsorption specific capacities in other samples of 50.8 mAh/g (3a), 53.2 mAh/g (3b) and 49.1 mAh/g (4a) and 47.7 mAh/g (4b) could be explained by the smaller crystallite size, resulting in a shorter diffusion path, which would lead to more rapid ionic transfer.[41,42] The lower water content of these samples in the crystal framework may also have contributed to the improved adsorption capacity as the water in the framework could occupy the intercalation sites.[20]
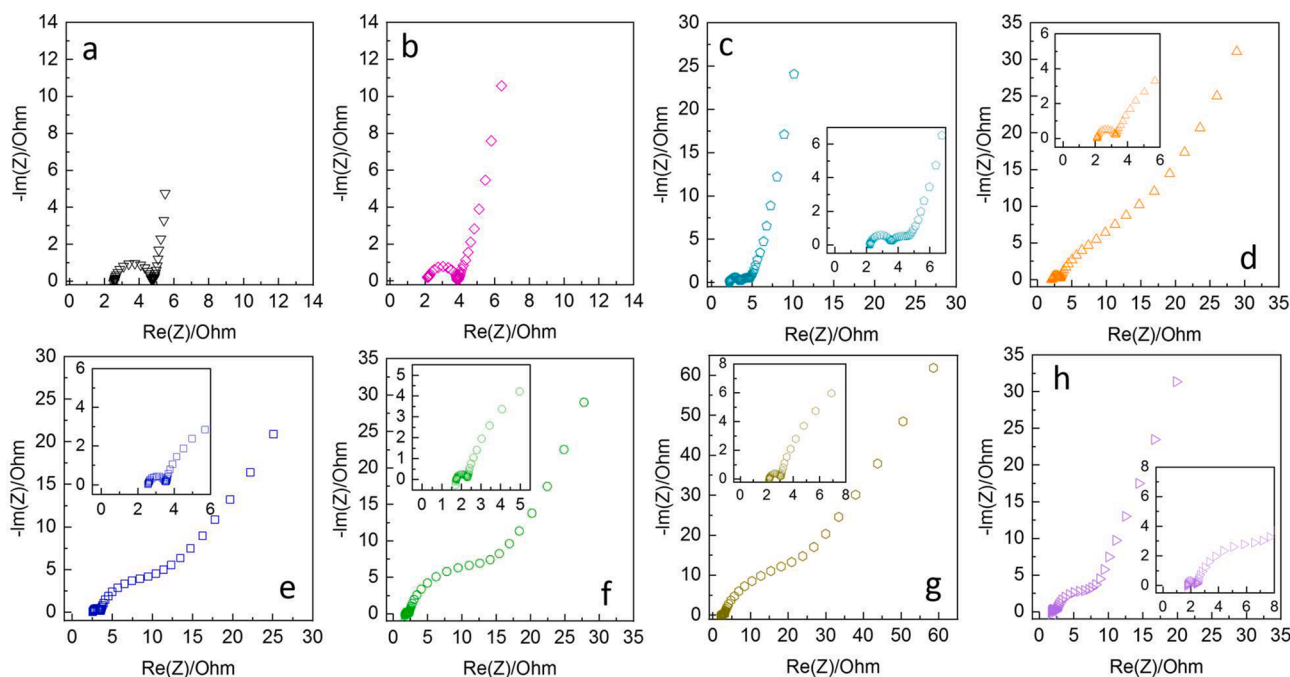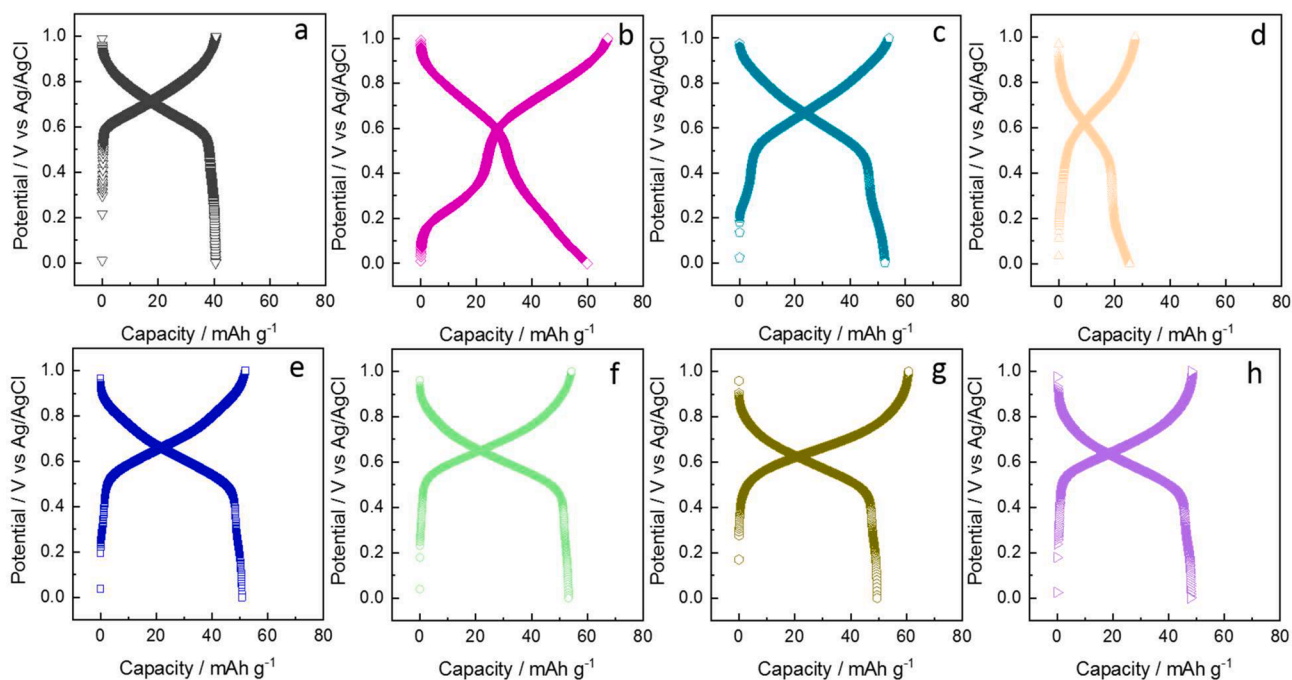

Fig. 5. Nyquist plots of CuHCF-based electrodes with each powder sample, inset is the enlarged curve in the high frequency region (a-sample 1, b-sample 2a, c-sample 2b, d-sample 2c, e-sample 3a, f-sample 3b, g-sample 4a and h-sample 4b).

Fig. 6. Galvanostatic charge and discharge profiles of CuHCF-based electrodes with each powder sample at 7 mA/30 mg in 1 M NaCl. The mass used for calculation of specific capacity and the applied current was the active material for all the CuHCF samples. (a-sample 1, b-sample 2a, c-sample 2b, d-sample 2c, e-sample 3a, f-sample 3b, g-sample 4a and h-sample 4b).

3.5. Assessment of improved stability and performance

The conditions and materials used for the preparation of Sample 2a resulted in the most stable electrode material and a charge to discharge efficiency of ~ 100% (Fig. 1). However, all samples showed some reduction in capacity retention over time. This decrease in capacity retention with the number of cycles might be due to the lack of coordinated water content in the CuHCF framework (Fig. 3 and Table S3). The coordinated water was reported to be beneficial to stability of the crystal structure of PBAs in an open framework.[13] Even though less total water content may have contributed to the improved adsorption capacity (Fig. 6),[39,40] such a relationship was not observed in cycling tests. This trade-off in performance is consistent with the previous studies that the enhanced sodium storage capacity for CuHCF electrodes is often accompanied by a decrease in structural stability.[43]

Other factors that could have contributed to the stability of Sample 2a include unconventional carbon–nitrogen vacancies that help to suppress iron leaching in PBAs.[44] Active metals leaching from PBAs can lead to a decay in performance due to a loss of the active sites and thus a drop in charge–discharge capacity.[21] Increased stability can also result from activation of the reversible Cu^{II}/Cu^{I} redox couple, as this second redox couple appears to improve the reversible Fe^{III}/Fe^{II} redox behavior(Fig. 4) and lead to more stable cycling performance (Fig. 1). However, there was little extra capacity contributed by the Cu^{II}/Cu^{I} redox reaction itself due to the smaller potential window (± 0.6 V) used in the flow cell BDI system compared to the half cell (± 1.0 V in Fig. 6). Coulombic efficiencies were also impacted, with a higher efficiency observed for sample 2 compared to other samples likely due to the enhanced reversible Fe^{III}/Fe^{II} redox reaction than others. The smaller coulombic efficiency in the initial several cycles might be due to the decomposition of zeolitic water in the CuHCF framework.[45]

4. Conclusions

The properties of CuHCF powders were highly dependent on different synthesis conditions that included a variety of precursor concentrations, metal oxidation states, presence of chelators, and addition of sodium ion salts. Analysis of the different synthesis conditions suggests that an increase of sodium concentration in the precursor could reduce the Cu–N bond distance and therefore the unit cell volume. The reduced oxidation state of iron (Fe^{2+} rather than Fe^{3+}) in the precursors always produced smaller crystallites. Addition of chelators reduced zeolitic and/or coordinated water contents in the CuHCF framework, which further affected the ion conduction within the solid material. The combination of smaller particle sizes and lower water contents in the CuHCF framework led to a higher initial sodium removal capacity due to the shorter diffusion length, and fewer water-occupied intercalation sites. However, the lower water contents adversely impacted BDI cycling stability as shown by a loss in capacity over time. The presence of coordinated water in the framework was helpful for increasing ion diffusion rates and could also provide beneficial vacancies to suppress active metal leaching. The activation of reversible Cu^{II}/Cu^{I} redox reaction was observed due to the coordination of chelators in precursor solutions, which contributed to a faster and more reversible Fe^{III}/Fe^{II} redox reaction and led to a more stable BDI cycling performance with long-term operation. These results therefore combined to produce the improved stability of 79.4% retention after 100 cycles for the conditions used in Sample 2a, compared to a range of 20–55% for the other samples.

Declaration of competing interest

The authors declare that they have no known competing financial interests or personal relationships that could have appeared to influence the work reported in this paper.

Acknowledgments

Appendix A. Supplementary data

Supplementary data to this article can be found online at https://doi.org/10.1016/j.cej.2022.135001.

References

[1] M.E. Suss, V. Presser, Water desalination with energy storage electrode materials, Joule 2 (1) (2018) 10–15.

[2] L. Wang, J.E. Dykstra, S. Lin, Energy efficiency of capacitive deionization, Environ. Sci. Technol. 53 (7) (2019) 3366–3378.

[3] S. Porada, R. Zhao, A. van der Wal, V. Presser, P.M. Biesheuvel, Review on the science and technology of water desalination by capacitive deionization, Prog. Mat. Sci. 58 (8) (2013) 1388–1442.

[4] X. Zhang, K. Zuo, X. Zhang, C. Zhang, P. Liang, Selective ion separation by capacitive deionization (cdi) based technologies: A state-of-the-art review, Environ. Sci. Water Res. Technol. 6 (2) (2020) 243–257.

[5] J.G. Gamaethiralalage, K. Singh, S. Sahin, J. Yoon, M. Elimelech, M.E. Suss, P. Liang, P.M. Biesheuvel, R.L. Zornitta, L.C.P.M. de Smet, Recent advances in ion selectivity with capacitive deionization, Energy Environ. Sci. 14 (3) (2021) 1095–1120.

[6] M.E. Suss, T.F. Baumann, W.L. Bourcier, C.M. Spadaccini, K.A. Rose, J.G. Santiago, M. Stadermann, Capacitive desalination with flow-through electrodes, Energy Environ. Sci. 5 (11) (2012) 9511–9519.

[7] R. Wang, S. Lin, Thermodynamic reversible cycles of electrochemical desalination with intercalation materials in symmetric and asymmetric configurations, J. Colloid Interface Sci. 574 (2020) 152–161.

[8] C. Kim, P. Srimuk, J. Lee, M. Aslan, V. Presser, Semi-continuous capacitive deionization using multi-channel flow stream and ion exchange membranes, Desalination 425 (2018) 104–110.

[9] C. Kim, J. Lee, P. Srimuk, M. Aslan, V. Presser, Concentration-gradient multichannel flow-stream membrane capacitive deionization cell for high desalination capacity of carbon electrodes, ChemSusChem 10 (24) (2017) 4914–4920.

[10] L. Wang, C. Zhang, C. He, T.D. Waite, S. Lin, Equivalent film-electrode model for flow-electrode capacitive deionization: Experimental validation and performance analysis, Water Res. 181 (2020), 115917.

[11] T. Kim, C.A. Gorski, B.E. Logan, Low energy desalination using battery electrode deionization, Environ. Sci. Technol. Lett 4 (10) (2017) 444–449.

[12] M. Son, V. Pothanamkandathil, W. Yang, J.S. Vrouwenvelder, C.A. Gorski, B. E. Logan, Improving the thermodynamic energy efficiency of battery electrode deionization using flow-through electrodes, Environ. Sci. Technol. 54 (6) (2020) 3628–3635.

[13] B. Wang, Y. Han, X. Wang, N. Bahlawane, H. Pan, M. Yan, Y. Jiang, Prussian blue analogs for rechargeable batteries, iScience 3 (2018) 110–133.

[14] K. Hurlbutt, S. Wheeler, I. Capone, M. Pasta, Prussian blue analogs as battery materials, Joule 2 (10) (2018) 1950–1960.

[15] G. Zampardi, M. Warnecke, M. Tribbia, J. Glenneberg, C. Santos, F. La Mantia, Effect of the reactants concentration on the synthesis and cycle life of copper hexacyanoferrate for aqueous zn-ion batteries, Electrochem. Commun. 126 (2021) 107030, https://doi.org/10.1016/j.elecom.2021.107030.

[16] S. Kjeldgaard, I. Dugulan, A. Mamakhel, M. Wagemaker, B.B. Iversen, A. Bentien, Strategies for synthesis of prussian blue analogues. *Royal Society Open*, Science 8 (1) (2021) 201779, https://doi.org/10.1098/rsos.201779.

[17] W. Wang, Y. Gang, Z. Hu, Z. Yan, W. Li, Y. Li, Q.-F. Gu, Z. Wang, S.-L. Chou, H.-K. Liu, S.-X. Dou, Reversible structural evolution of sodium-rich rhombohedral prussian blue for sodium-ion batteries, Nat. Commun. 11, (1) (2020) 980.

[18] Y. Xu, J. Wan, L. Huang, J. Xu, M. Ou, Y. Liu, X. Sun, S. Li, C. Fang, Q. Li, J. Han, Y. Huang, Y. Zhao, Dual redox-active copper hexacyanoferrate nanosheets as cathode materials for advanced sodium-ion batteries, Energy Storage Mater. 33 (2020) 432–441.

[19] Z. Song, W. Liu, X. Wei, Q. Zhou, H. Liu, Z. Zhang, G. Liu, Z. Zhao, Charge storage mechanism of copper hexacyanoferrate nanocubes for supercapacitors, Chin. Chem. Lett. 31 (5) (2020) 1213–1216.

[20] W.-J. Li, C. Han, G. Cheng, S.-L. Chou, H.-K. Liu, S.-X. Dou, Chemical properties, structural properties, and energy storage applications of prussian blue analogues, Small 15 (32) (2019) 1900470, https://doi.org/10.1002/smll.v15.3210.1002/smll.201900470.

[21] L. Shi, E. Newcomer, M. Son, V. Pothanamkandathil, C.A. Gorski, A. Galal, B. E. Logan, Metal-ion depletion impacts the stability and performance of battery electrode deionization over multiple cycles, Environ. Sci. Technol. 55 (8) (2021) 5412–5421.

[22] R. Gao, L. Bonin, J.M.C. Arroyo, B.E. Logan, K. Rabaey, Separation and recovery of ammonium from industrial wastewater containing methanol using copper hexacyanoferrate (cuhcf) electrodes, Water Res. 188 (2021), 116532.

[23] V. Pothanamkandathil, J. Fortunato, C.A. Gorski, Electrochemical desalination using intercalating electrode materials: A comparison of energy demands, Environ. Sci. Technol. 54 (6) (2020) 3653–3662.

[24] D.O. Ojwang, J. Grins, D. Wardecki, M. Valvo, V. Renman, L. Häggström, T. Ericsson, T. Gustafsson, A. Mahmoud, R.P. Hermann, G. Svensson, Structure characterization and properties of k-containing copper hexacyanoferrate, Inorg. Chem. 55 (12) (2016) 5924–5934.

[25] V. Renman, D.O. Ojwang, M. Valvo, C.P. Gómez, T. Gustafsson, G. Svensson, Structural-electrochemical relations in the aqueous copper hexacyanoferrate-zinc system examined by synchrotron x-ray diffraction, J. Power Sources 369 (2017) 146–153.

[26] J. Li, L. He, J. Jiang, Z. Xu, M. Liu, X. Liu, H. Tong, Z. Liu, D. Qian, Facile syntheses of bimetallic prussian blue analogues (kxm[fe(cn)6]·nh2o, m=ni, co, and mn) for electrochemical determination of toxic 2-nitrophenol, Electrochim. Acta 353 (2020) 136579, https://doi.org/10.1016/j.electacta.2020.136579.

[27] C. Zhang, Y. Xu, M. Zhou, L. Liang, H. Dong, M. Wu, Y. Yang, Y. Lei, Potassium prussian blue nanoparticles: A low-cost cathode material for potassium-ion batteries, Adv. Funct. Mater. 27, (4) (2017) 1604307.

[28] D. Yang, J. Xu, X.-Z. Liao, H. Wang, Y.-S. He, Z.-F. Ma, Prussian blue without coordinated water as a superior cathode for sodium-ion batteries, Chem. Commun. 51 (38) (2015) 8181–8184.

[29] L. Samain, F. Grandjean, G.J. Long, P. Martinetto, P. Bordet, D. Strivay, Relationship between the synthesis of prussian blue pigments, their color, physical properties, and their behavior in paint layers, J. Phys. Chem. C 117 (19) (2013) 9693–9712.

[30] D. Asakura, C.H. Li, Y. Mizuno, M. Okubo, H. Zhou, D.R. Talham, Bimetallic cyanide-bridged coordination polymers as lithium ion cathode materials: Core@shell nanoparticles with enhanced cyclability, J. Am. Chem. Soc. 135 (7) (2013) 2793–2799.

[31] X. Wu, J.J. Hong, W. Shin, L.u. Ma, T. Liu, X. Bi, Y. Yuan, Y. Qi, T.W. Surta, W. Huang, J. Neuefeind, T. Wu, P.A. Greaney, J. Lu, X. Ji, Diffusion-free grotthuss topochemistry for high-rate and long-life proton batteries, Nat. Energy 4 (2) (2019) 123–130.

[32] Y. Jiang, J. Liu, Definitions of pseudocapacitive materials: A brief review, Energy Environ. Mater. 2 (1) (2019) 30–37.

[33] X. Dong, Y. Yang, B. Wang, Y. Cao, N. Wang, P. Li, Y. Wang, Y. Xia, Low-temperature charge/discharge of rechargeable battery realized by intercalation pseudocapacitive behavior, Adv. Sci. 7, (14) (2020) 2000196.

[34] X. Yang, A.L. Rogach, Electrochemical techniques in battery research: A tutorial for nonelectrochemists, Adv. Energy Mater. 9, (25) (2019) 1900747.

[35] X. Pu, D. Zhao, C. Fu, Z. Chen, S. Cao, C. Wang, Y. Cao, Understanding and calibration of charge storage mechanism in cyclic voltammetry curves, Angew. Chem. Int. Ed. 60 (39) (2021) 21310–21318.

[36] R.R. Gaddam, L. Katzenmeier, X. Lamprecht, A.S. Bandarenka, Review on physical impedance models in modern battery research, Phys. Chem. Chem. Phys. 23 (23) (2021) 12926–12944.

[37] C. Ho, I.D. Raistrick, R.A. Huggins, Application of a-c techniques to the study of lithium diffusion in tungsten trioxide thin films, J. Electrochem. Soc. 127 (2) (1980) 343–350.

[38] C.D. Wessells, S.V. Peddada, M.T. McDowell, R.A. Huggins, Y. Cui, The effect of insertion species on nanostructured open framework hexacyanoferrate battery electrodes, J. Electrochem. Soc. 159 (2) (2011) A98–A103.

[39] M. Fiore, S. Wheeler, K. Hurlbutt, I. Capone, J. Fawdon, R. Ruffo, M. Pasta, Paving the way toward highly efficient, high-energy potassium-ion batteries with ionic liquid electrolytes, Chem. Mater. 32 (18) (2020) 7653–7661.

[40] G. He, L.F. Nazar, Crystallite size control of prussian white analogues for nonaqueous potassium-ion batteries, ACS Energy Lett. 2 (5) (2017) 1122–1127.

[41] W. Ren, M. Qin, Z. Zhu, M. Yan, Q. Li, L. Zhang, D. Liu, L. Mai, Activation of sodium storage sites in prussian blue analogues via surface etching, Nano Lett. 17 (8) (2017) 4713–4718.

[42] Y. Huang, M. Xie, J. Zhang, Z. Wang, Y. Jiang, G. Xiao, S. Li, L. Li, F. Wu, R. Chen, A novel border-rich prussian blue synthetized by inhibitor control as cathode for sodium ion batteries, Nano Energy 39 (2017) 273–283.

[43] M. Okubo, D. Asakura, Y. Mizuno, T. Kudo, H. Zhou, A. Okazawa, N. Kojima, K. Ikedo, T. Mizokawa, I. Honma, Ion-induced transformation of magnetism in a bimetallic cufe prussian blue analogue, Angew. Chem. Int. Ed. 50 (28) (2011) 6269–6273.

[44] Z.-Y. Yu, Y. Duan, J.-D. Liu, Y. Chen, X.-K. Liu, W. Liu, T. Ma, Y. Li, X.-S. Zheng, T. Yao, M.-R. Gao, J.-F. Zhu, B.-J. Ye, S.-H. Yu, Unconventional cn vacancies suppress iron-leaching in prussian blue analogue pre-catalyst for boosted oxygen evolution catalysis, Nat. Commun. 10, (1) (2019) 2799.

[45] Y.a. You, X. Yu, Y. Yin, K.-W. Nam, Y.-G. Guo, Sodium iron hexacyanoferrate with high na content as a na-rich cathode material for na-ion batteries, Nano Res. 8 (1) (2015) 117–128.